ChemPhysMater xxx (xxxx) xxx

Contents lists available at ScienceDirect

ChemPhysMater

journal homepage: www.elsevier.com/locate/chphma

Aggregation properties of a therapeutic peptide for rheumatoid arthritis: A spectroscopic and molecular dynamics study

Rita Cimino[a], Marco Savioli[a], Noemi Ferrante Carrante[a], Ernesto Placidi[c], Hilda Garay-Perez[d], Matilde López-Abad[d], Alexis Musacchio Lasa[d], Maria Del Carmen Domínguez-Horta[d], Emanuela Gatto[a], Francesca Cavalieri[a,b,*], Gianfranco Bocchinfuso[a], Mariano Venanzi[a,*]

[a] PEPSA-LAB, Department of Chemical Sciences and Technology, University of Rome Tor Vergata, Via della Ricerca Scientifica 1, 00133, Rome, Italy
[b] School of Science, RMIT University, Melbourne, VIC 3001, Australia
[c] Department of Physics, University of Rome 'Sapienza', P.le A. Moro 5, 00185 Rome, Italy
[d] Centre for Genetic Engineering and Biotechnology, PO Box 6162, 10600, Havana, Cuba

ARTICLE INFO

Keywords:
Molecular dynamics of peptide oligomers
Peptide aggregation
Peptide fibrils
Peptide nanostructures
Therapeutic peptides
Treatment of rheumatoid arthritis

ABSTRACT

The biological properties of therapeutic peptides, such as their pharmacokinetics and pharmacodynamics, are correlated with their structure and aggregation properties. Herein, we studied the aggregation properties of a therapeutic peptide (CIGB-814), currently in phase 2 clinical trial, for the treatment of rheumatoid arthritis over a wide range of concentrations (μM–mM). We applied spectroscopic techniques (fluorescence, circular dichroism, resonance, and dynamic light scattering), atomic force microscopy, and molecular dynamics simulations to determine the aggregation mechanism of CIGB-814. We found that the hierarchical aggregation of CIGB-814 at micromolar concentrations was initiated by the formation of peptide oligomers. Subsequently, the peptide oligomers trigger the nucleation and growth of peptide nanostructures (cac = 123 μM), ultimately leading to the fibrillization of CIGB-814 (cac' = 508 μM). These results pave the way for a deeper understanding of the CIGB-814 therapeutic activity and may give important insights on its pharmacokinetics.

1. Introduction

Rheumatoid arthritis (RA) is an autoimmune disease that affects 0.3–1% of the global population and represents the major cause of disability among older people in Western countries. Unfortunately, currently, only palliative treatments that do not cure the disease are available to improve the quality of life of RA patients.

Standard therapies are based on disease-modifying antirheumatic drugs (DMARDs) and methotrexate [1]. Biologics are alternative drugs for patients who do not respond to DMARDs. However, 40–50% of RA patients have a limited response to these drugs [2].

Antigen-specific therapy could represent a suitable approach for those who exhibit resistance to traditional treatments. This approach aims to eliminate only T cells that have evaded the control mechanisms of peripheral tolerance [3]. The central role of T cells in the pathogenesis of RA is well established. Under physiological conditions, the induction of antigen-specific tolerance is required for immune homeostasis and the control of autoreactive T cells that cause the onset of autoimmune diseases [4].

In the case of RA, it is crucial to control the expression of interleukins 17 (IL-17) and interferon-γ (IFN-γ) [5]. IL-17 is produced by T_h cells. These cells play an important role in many inflammatory diseases, including RA. Under high IL-17 levels, the conditions of RA patients worsen dramatically. In contrast, IFN-γ, a T_{h1} cell product, promotes the elimination of many intracellular pathogens. However, its overexpression may cause many autoimmune diseases [5]. Anti-cyclic citrullinated peptides (anti-CCP) are a biomarker of RA; they are autoantibodies that exert their inhibitory action against citrullinated proteins, mostly present in patients affected by RA.

A new heat shock protein 60 (HSP60) peptide epitope, consisting of 27-residue long sequence SIDLKDKYKNIGAKLVQLVANNTNEEA-NH_2, denoted as CIGB-814, was recently synthesized at the Center for Genetic Engineering and Biotechnology (CIGB), Havana (Cuba). The single-site Leu→Asp-substitution was introduced into the new peptide analog as it strongly increased the affinity of CIGB-814 for human leukocyte antigen gene complex-II by inhibiting the activation of T cells and stimulating the production of regulatory cells that can suppress the activity of $CD4^+$ cells [6].

CIGB-814 has recently been used in clinical phase 2 studies. During phase 1, CIGB-814 showed positive results in the treatment of RA patients, causing a marked decrease in the production of IL-17, IFN-γ, and anti-CCP. Importantly, these results were accompanied with a general improvement in the quality of life of patients involved in this early phase

* Corresponding author.
E-mail address: venanzi@uniroma2.it (M. Venanzi).

https://doi.org/10.1016/j.chphma.2021.09.007
Received 5 August 2021; Received in revised form 16 September 2021; Accepted 16 September 2021
Available online xxx

Please cite this article as: R. Cimino, M. Savioli, N.F. Carrante et al., Aggregation properties of a therapeutic peptide for rheumatoid arthritis: A spectroscopic and molecular dynamics study, ChemPhysMater, https://doi.org/10.1016/j.chphma.2021.09.007

[7,8]. In clinical phase 2 studies, patients received a subcutaneous dose (between 0.5 and 5 mg) for 5 months.

The mechanism of action of CIGB-814 has been studied in vitro and in two animal models. The therapeutic effect of CIGB-814 in animal models is attributed to the processing and presentation of this altered peptide ligand by dendritic cells to T-lymphocytes in the intestine or lymph nodes, inducing the expression of regulatory T cells (Tregs). These activated cells migrate to the inflammation site and can cross-recognize wild type epitopes from HSP60, which is highly expressed due to the inflammation process. This new contact with HSP60 autoantigen may induce potent immunoregulatory effects, attenuating autoreactive T cells responsible for RA pathogenesis and inhibiting inflammatory processes.

Interestingly, clinical trial studies have suggested that the aggregation state of CIGB-814 can influence the experimental analysis and affect treatment efficacy. The aggregation of CIGB-814 can be induced by several formulation factors including ionic strength, pH, additives, and peptide concentration; therefore, it is crucial to study the aggregation properties of CIGB-814 in different environments to optimize the drug efficacy and administration route.

In this study, we sought to investigate the unexplored aggregation properties of CIGB-814. Aggregation is a common problem that affects the formulation development and pharmaceutical processing of peptides, often leading to loss of bioactivity and enhanced autoimmune response [9]. It is known that most therapeutic peptides form irreversible aggregates over time during storage, transport, or administration to patients [10,11]. In particular, age-dependent aggregation is irreversible, and aged aggregates do not dissociate upon dilution or pH changes. Small irreversible aggregates may represent the nuclei of subsequent growth stages, which, following multiple pathways (monomer addition and aggregate fusion), can lead to the formation of soluble nanostructures, and ultimately to phase separation [12]. In contrast, aggregated peptides are expected to be more immunogenic than their parent monomers. Hence, peptide aggregates can be designed as vaccines, where immunogenicity is highly desirable [13]. In addition, some peptides can exert their biological activity as oligomers, losing bioactivity after dissociation [14]. These considerations highlight the need for in-depth investigation of the aggregation properties of a new peptide drug, which is a crucial step for developing a formulation with optimal pharmacokinetics, product stability, and long shelf life.

In this study, we report the aggregation properties of CIGB-814 by applying optical spectroscopy (UV–vis absorption, circular dichroism (CD), and fluorescence), resonance and dynamic light scattering, atomic force microscopy (AFM), and molecular dynamics (MD) simulations. This study will potentially pave the way for the development of CIGB-814 as a specific antigenic drug and an innovative and more effective therapeutic approach for RA.

2. Materials and methods

2.1. Materials

Abbreviations. DIC, N,N′−1,3-diisopropylcarbodiimide; DIEA, N,N-diisopropylethylamine; DMF, N,N-dimethylformamide; ESI-MS, electrospray ionization mass spectrometry; Fmoc/tBu 9-fluorenylmethyloxycarbonyl/tert-butyl; Fmoc-AM(p-[(R,S)-a-[1-(9H-*fluoren*-9-*yl*)*methoxy-formamido*]−2,4-dimethyl-benzyl] phenoxyacetic acid; HPLC, high-performance liquid chromatography; MBHA, 4-methylbenzhydrylamine; Q-TOF2, quadrupole-time of-flight; RP, reverse phase; TFA, trifluoroacetic acid; TIS, triisopropylsilane.

CIGB-814 was synthesized at the Center for Genetic Engineering and Biotechnology (Havana, Cuba).

Peptide synthesis. The CIGB-814 peptide was synthesized manually on Fmoc-AM-MBHA resin by a stepwise solid-phase procedure using the Fmoc/tBu strategy [15]. The Fmoc group was removed with 20% piperidine in DMF. The Fmoc-amino acids were coupled using DIC/OxymaPure activation, and the completion of the coupling reaction was monitored using the ninhydrin test. Side-chain release and cleavage from the resin were performed by treatment with TFA-H_2O-TIS (95:2.5:2.5 v/v) for 2 h. Thereafter, the peptide was precipitated with cold ether, dissolved in 40% acetonitrile/H_2O, and freeze-dried. The crude peptide was purified using reversed-phase high-performance liquid chromatography (RP-HPLC), and its identity was confirmed using ESI-MS. CIGB-814 of more than 97% purity was obtained, as ascertained using analytical RP-HPLC. The molecular mass determined experimentally via ESI-MS corresponded with the theoretically calculated monoisotopic mass (2986.6 Da).

Chromatography. The purity of CIGB-814 was determined using an AKTA 100 HPLC system (GE Healthcare, USA). Analytical separation was achieved using a reverse-phase (RP) C18 column (4.6 × 150 mm, 5 μm) (Vydac, USA). A linear gradient from 5 to 60% of solvent B over 35 min at a flow rate of 0.8 mL/min was used. Solvent A: 0.1% TFA in water and solvent B: 0.05% TFA in acetonitrile. The chromatogram was obtained at 226 nm using the UNICORN 5.31 (GE Healthcare USA) software package for data processing. The preparative purification was performed on an AKTA 10 HPLC system (GE Healthcare, USA). Separation was achieved using an RP C18 column (Vydac, 50 × 250 mm, 20 μm). A linear gradient from 20 to 40% of solvent B over 60 min at a flow rate of 50 mL/min was used. Detection was achieved at a wavelength of 226 nm. Solvent A: 0.1% (v/v) TFA in water and solvent B: 0.05% (v/v) of TFA in acetonitrile.

Mass Spectrometry. ESI-MS was performed using a hybrid quadrupole-time-of-flight (Q-TOF2) instrument (Waters, Milford, MA, USA) fitted with a nanospray ion source. The capillary and cone voltages were set to 900 and 35 V, respectively. Data withdrawal and processing were performed using the MassLynx (version 4) package (Waters, USA).

2.2. Methods

UV–Vis absorption spectroscopy. UV–Vis absorption measurements were carried out at 25 °C in the 200–400 nm wavelength range using a Varian Cary 100 Scan spectrophotometer equipped with a Peltier thermostat, using quartz cells (1 cm).

Fluorescence spectroscopy. Steady-state emission spectra were measured at 25 °C using a Fluoromax-4 spectrofluorometer (Horiba Jobin Yvon) equipped with automatically controlled Glan-Thomson polarizers and operated with single-photon counting detection. Emission spectra were acquired using quartz cells (0.4 × 1 cm), λ_{ex} = 270 nm, λ_{em} = 285–400 nm, with 0.5 s/nm integration time. Entrance and exit (e/e) slits were adjusted depending on the concentration of the solution, i.e., 2/5 nm in the 2–300 μM concentration range and 1/3 nm for 0.5–0.8 mM aqueous solutions.

Pyrene assay. The pyrene assay is based on the ratio between the first (λ = 372 nm) and third (λ = 383 nm) vibronic components of the $S_1 \rightarrow S_0$ pyrene emission band [16]. This ratio was shown to be sensitive to the pyrene environment, making this dye suitable for aggregation studies. For the pyrene assay, a 1 × 1 cm quartz cell, λ_{ex} = 310 nm, λ_{em} = 350–600 nm, 1 s/nm integration time, and 3/3 nm e/e slits. Pyrene solution concentration was 2 μM.

Thioflavin assay. A thioflavin (ThT) assay (Fluka, Büchs, Switzerland) was carried out in a water solution with ThT 2 μM and with peptide concentrations ranging from 60 μM to 1 mM, using a quartz cuvette (0.4 × 1 cm). The spectra were collected at λ_{em} = 450–565 nm, exciting at λ_{ex} = 430 nm.

Fluorescence anisotropy. The fluorescence anisotropy coefficient r was determined using the equation:

$$r = \frac{I_{\parallel} - I_{\perp}}{I_{\parallel} + 2I_{\perp}}$$

where $I_{\parallel}$ and $I_{\perp}$ are, respectively, the intensities of the emission in parallel or perpendicular polarization with respect to the polarization of the incident radiation [17]. For parallel absorption and emission dipoles,

$r = r_{max} = 0.4$ for an ensemble of randomly oriented fluorophores. Fluorescence anisotropy measurements were carried out using a 0.4 × 1 cm quartz cell, λ_{ex} = 270 nm, λ_{em} = 320 nm, integration time of 10 s/nm, and slits of 5/5 nm.

Time-resolved fluorescence. Time-resolved fluorescence results are modeled using a multiexponential time decay function [18]:

$$I(t) = \sum_i \alpha_i \, e^{-\frac{t}{\tau_i}}$$

The α_i and τ_i parameters were obtained using an iterative deconvolution method by applying non-linear least-squares analysis. Experimental parameters: λ_{ex} = 282 nm, λ_{em} = 330 nm, and 1/1 nm e/e slit. A 295 nm cutoff filter was used to minimize diffuse light contamination.

CD. CD spectra were measured using a J800 spectropolarimeter (Jasco) at 25 °C (Peltier). Experimental parameters: 0.1 cm quartz cell, wavelength range 190–250 nm, 2 nm bandwidth, 1 s/nm integration time.

Resonance (Rayleigh) light scattering (RLS). RLS experiments were carried out with the same Fluoromax-4 spectrofluorometer as described above, in continuous mode (resonance conditions) using a 0.4 × 1 cm quartz cell, $\lambda_{ex}/\lambda_{em}$ = 240–600 nm, 1 s/nm integration time, and 1.5/1.5 nm e/e slits.

Dynamic light scattering (DLS). The particle size distribution of CIGB-814 in solution was measured using DLS with a Delsa Nano C Particle Analyzer (Beckman Coulter, USA). The CIGB-814 peptide was reconstituted in water for injection at a concentration of 800 μM. DLS measurements of the samples were carried out over time after reconstitution of the peptide in MilliQ water.

AFM. AFM measurements were carried out in tapping mode using a Veeco Multimode Nanoscope IIIa with a Si tip (k = 40 N/m, curvature radius = 7 nm). Samples were prepared by dipping 1 μL of peptide aqueous solution at 0.1 mg/mL (≈ 33.5 μM) and 1.8 mg/mL (≈ 600 μM) concentrations on a freshly cleaved mica surface. The solution/mica system was incubated overnight and dried under gentle Ar flux.

MD simulations. MD simulations were performed using the GROMACS package version 2019.6 [19] and the GROMOS 54a7-FF force field [20]. To investigate the peptide conformational properties and the nucleation of the aggregation process, MD simulations with one (MD1), three (MD3), six (MD6), and nine (MD9) molecules were carried out in a 10 mM NaCl aqueous solution. A time step of 2 fs was used for equilibration and production runs. The equilibrium temperature (300 K) was controlled via velocity rescaling with a coupling constant of 0.1 ps [21]. The pressure was controlled by an isotropic Parrinello-Rahman barostat with a coupling constant of 2 ps and a reference external pressure of 1 atm [22]. Lennard-Jones long-range interactions were treated with a cutoff radius of 1.2 nm. Coulombic interactions were calculated using the particle mesh Ewald method [23]. The LINCS algorithm was used to constrain all bond lengths during the MD simulations [24]. Three replicas of each system were performed for 500 ns simulations with different starting configurations. MD simulation analyses were carried out using built-in GROMACS tools and Vega ZZ [25]. Secondary structure content was assessed using the Dictionary Secondary Structure of Proteins (DSSP) algorithm [26]. To determine the oligomerization state in MD3, MD6, and MD9, a Python script was employed, considering a peptide pair as part of an oligomer when at least two atoms from the two peptides are closer than 0.4 nm. The MD experimental conditions are summarized in the Supplementary Information (SI, Table SIT1).

3. Results and discussion

3.1. Spectroscopy

UV–Vis absorption. The near-UV absorption spectra of CIGB-814 aqueous solutions in the concentration range of 4.6–837 μM are shown in Figure S1. The acquired spectra were characterized by an unstructured absorption band that peaked at λ = 270 nm, which is typical of the Tyr-phenol group. From these results, the molar extinction coefficient of CIGB-814 [ε(280) = 1430 M^{-1}•cm^{-1}] at λ = 280 nm was determined, which is in good agreement with the literature data [ε(280 nm) = 1490 M^{-1}•cm^{-1}] [27].

The linearity of the absorbance versus concentration plot (Figure SI2) suggests that the UV absorption spectra of CIGB-814 are not perturbed by intermolecular effects in the concentration range investigated. However, the absorption spectra of CIGB-814 aqueous solutions after one week showed changes in the spectral characteristics, signaling the occurrence of aggregation phenomena over a long period (Figure SI3).

Fluorescence spectroscopy. The emission spectra of CIGB-814 in the 4.6–837 μM concentration range (Figure SI4) are typical of the Tyr-residue. These data and the plot of the emission intensity at $\lambda_{em,max}$ = 306 nm versus the CIGB-814 concentration (Figure SI5) indicate that the fluorescence intensities increase proportionally to the peptide concentration up to 300 μM. At higher concentrations, a substantial quenching of the Tyr-emission was observed, suggesting the occurrence of aggregation phenomena promoted by long-range weak interactions. It should be noted that, in the same concentration range, the absorption spectra of fresh peptide solutions were not perturbed by such weak interactions. To better characterize the peptide aggregation process, we carried out two fluorescence assays based on pyrene and thioflavin emissions.

The pyrene assay is based on the dependence of the pyrene emission spectrum on the polarity of the environment. Specifically, the ratio between the first (I_1, λ_{em} = 372 nm) and third (I_3, λ_{em} = 383 nm) vibronic component of the $S_1 \rightarrow S_0$ pyrene emission was found to be very sensitive to the environmental polarity, allowing for the determination of the critical aggregation concentration (cac) of nanostructures [16].

In Figs. 1A and 1B, the emission spectra of 2 μM pyrene aqueous solution obtained by adding increasing aliquots of CIGB-814, and the I_1/I_3 ratio as a function of the peptide concentration (log) are reported. In Fig. 1B, two different regions of the I_1/I_3 ratio on the CIGB-814 concentration can be easily identified. The crossing point of the two linear regions indicates the transfer of the pyrene fluorophore from the aqueous solution to the apolar inner core of the peptide aggregates [28]. From the data reported in Fig. 1B, cac = 123 μM (log[CIGB-814]=−3.91) can be determined. The absence of pyrene excimer emission allowed us to rule out the contribution of pyrene-pyrene interactions to the observed variation of the I_1/I_3 ratio, indicating that single pyrene molecules are embedded in the peptide nanostructures [29].

The thioflavin T (ThT) assay is based on the increase in ThT fluorescence emission upon binding to peptide nanostructures [30]. As ThT is claimed to selectively bind to β-sheet conformation, this assay has been largely applied to the detection of amyloid structures and peptide fibrils [31,32]. Therefore, we carried out a fluorescence titration experiment by adding CIGB-814 aliquots to a micromolar ThT solution (Fig. 2).

By reporting the ThT emission intensities at λ_{em} = 480 nm as a function of the peptide concentration (log), two linear regions can be identified (Fig. 2B). The crossing point of the two linear regions can be considered as the onset of the formation of β-sheet structures, corresponding to a second critical concentration point (cac'). From the data reported in Fig. 2B, we obtained cac' = 508 μM (log[CIGB-814] = −3.29).

Time-resolved fluorescence experiments (Table SIT2) showed that for peptide concentrations less than 10 μM, Tyr-time decay is accounted for by a three-exponential function. In contrast, in the 20–317 μM range, Tyr-emission decay is stably accounted for by two lifetimes, with a constant average decay time of approximately 2.1 ns. The multiexponential fluorescence intensity time decay of Tyr-has been interpreted in terms of ground-state rotamer equilibria [33], assuming that the interconversion kinetics among the conformational excited states are slower than the fluorescence decay kinetics [34]. This finding strongly suggests that at higher concentrations, the tyrosine group is embedded in a homogenous environment and experiences restricted dynamics [35].

Concentration-dependent fluorescence anisotropy measurements showed that the anisotropy coefficient (r) of Tyr-residue is 0.04 for

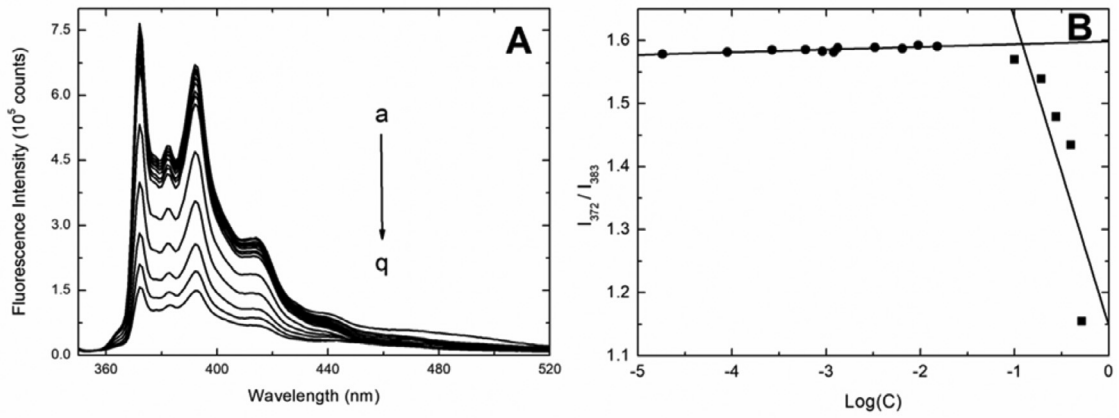

Fig. 1. (A) Pyrene emission spectra (2 μM, aqueous solutions) by adding aliquots of CIGB-814 from 0 (a) to 520 μM (q). (B) Intensity ratio of the I_1 (λ_{em} = 372 nm) vs. I_3 (λ_{em} = 383 nm) vibronic components of the Pyrene emission ($S_1 \rightarrow S_0$) as a function of the CIGB-814 molar concentration.

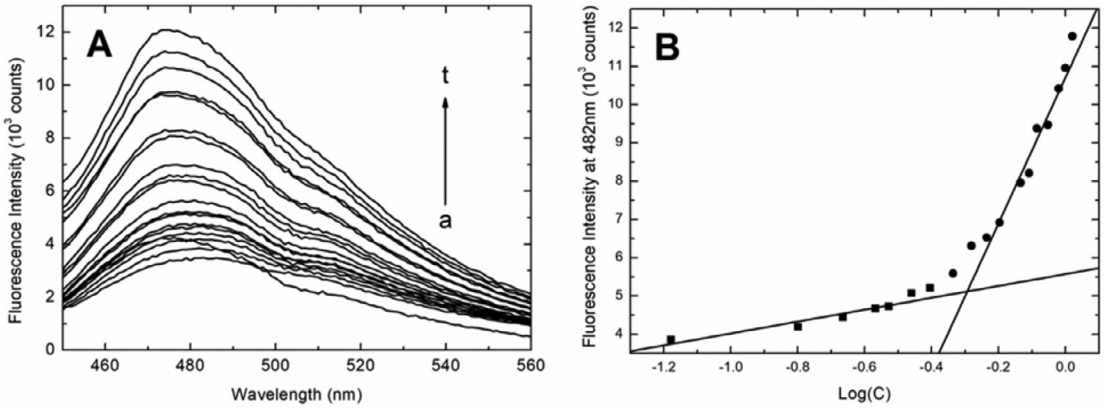

Fig. 2. Thioflavine (ThT) assay. (A) Fluorescence intensity of ThT on addition of increasing aliquots of CIGB-814 from 0 (a) to 1 mM (t). (B) Determination of the critical concentration for the formation of β-sheet structures (cac' = 508 μM) from ThT assay.

CIGB-814 at 2.3 μM, increases to 0.08 at 4.6 μM, and then stably maintains an asymptotic value of r = 0.11 from 9.2 to 837 μM (Table SIT3). This behavior revealed that the fluorescence emission time decay of Tyr-depended on the peptide concentration.

Lakowicz et al. [36] studied the fluorescence anisotropy time decay of a Tyr-containing octapeptide. They found that the anisotropy time decay can be described in terms of a fast lifetime component (ϑ_1 = 29 ps), associated with the local rotation of the fluorophore, and a slower lifetime (ϑ_2 = 454 ps), associated with the overall rotation of the peptide. For the two lifetimes, there are limit anisotropies, that is, the anisotropy coefficient at t = 0, of r_{01} = 0.208 and r_{02} = 0.112, corresponding to a total limit anisotropy $r_0 = r_{01} + r_{02}$ = 0.320.

From this value of r_0, the average lifetime (<τ>, Table SIT2), and the experimental anisotropy coefficient (Table SIT3), we can estimate the rotational correlation time of Tyr-as a function of the CIGB-814 concentration. We obtained 90 ps at 2.3 μM, 410 ps at 4.6 μM, and 1.10 ns for concentrations higher than 10 μM.

Overall, we can conclude that in the case of CIGB-814, the anisotropy coefficient at very low concentrations (below 10 μM) is depolarized by both the local rotational motion of the Tyr-phenol side chain and the overall rotational motion of the peptide monomer. Although the formation of CIGB-814 oligomers slows down the overall rotation of the peptide, it still leaves the local motion of the fluorophore unhindered, giving rise to a constant anisotropy coefficient $r = r_{02}$ = 0.11.

These results reveal the occurrence of a discontinuity point at a peptide concentration of 10 μM, which is an order of magnitude lower than the concentration range explored for the formation of peptide nanostructures (few hundreds of μM, from fluorescence experiments and the pyrene assay) and β-sheet formation (above 500 μM, from ThT assay). This third discontinuity point is associated with the insurgence of the reduced mobility of the Tyr-phenol group. This evidence is likely associated with the formation of CIGB-814 oligomers, which slows down the overall rotational motion of the peptide chains.

CD experiments were carried out in the 5–320 μM concentration range. Fig. 3 shows that in the concentration range up to 80 μM, the peptide maintained a predominant random coil conformation (Fig. 3A). However, at higher concentrations, a substantial redshift of the CD curves from 198 to 207 nm was observed (Fig. 3B), suggesting the presence of a population of ordered structures, in agreement with the results obtained by the pyrene assay (cac = 123 μM). This conformational transition triggers the formation of extended β-sheet structures, which were also detected by the ThT assay at higher peptide concentrations. Interestingly, the CD curves reported in Fig. 3B resemble the CD profile of the intermediate structures observed during the formation of amyloid fibers [37].

RLS experiments can be carried out to investigate the formation of aggregates of size comparable to the interrogating wavelength. Upon the formation of mesoscopic aggregates and under resonance conditions with the absorption transition, the intensity of the diffuse light is dramatically enhanced [38].

In Fig. 4, we report the RLS spectra of CIGB-814 in the 18.3–669 μM range. The data show a marked enhancement of the diffuse light intensity when the peptide concentration increased from 293 to 669 μM, in fair agreement with the results obtained by the ThT aggregation assay

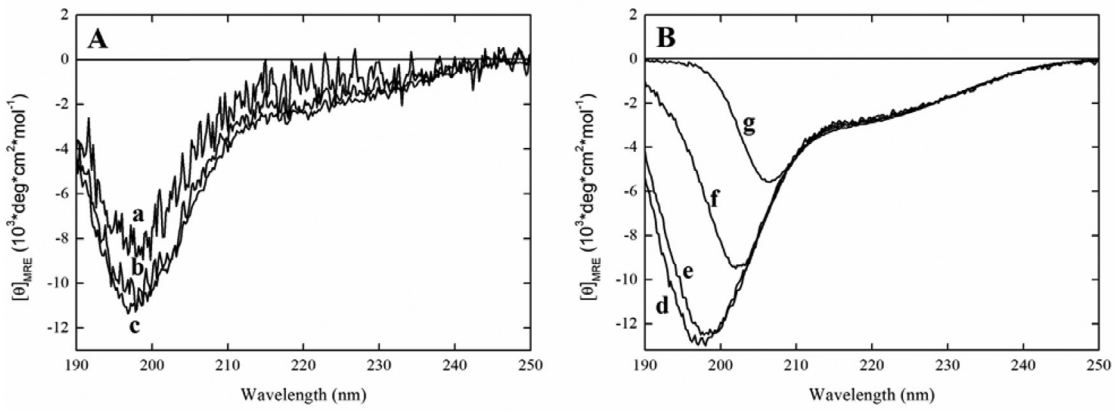

Fig. 3. Circular dichroism spectra of CIGB-814 aqueous solutions. (A) a: 5 μM; b: 10 μM; c: 20 μM. (B) d: 40 μM; e: 80 μM; f: 160 μM; g: 320 μM.

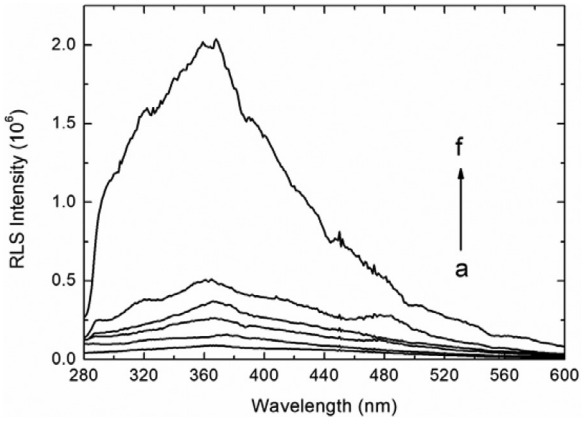

Fig. 4. Resonance Light Scattering spectra of CIGB-814 at different molar concentrations: (a) pure water; (b) 18.3 μM; (c) 73.3 μM; (d) 147 μM; (e) 293 μM; (f) 669 μM.

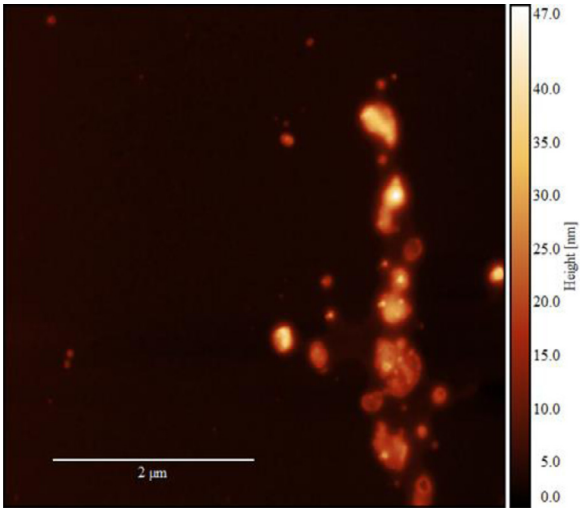

Fig. 5. AFM imaging of CIGB-814 on mica. Deposition solution concentration: 0.1 mg/mL (≈ 33.5 μM).

Table 1
Average Diameter of CIGB-814 aggregates from DLS experiments at different concentrations (μM) and times (h).

Concentration [μM]	Diameter [nm]		
	t_1 = 0 h	t_2 = 72 h	t_3 = 96 h
6	n.d*.	n.d.*	n.d.*
60	n.d*.	n.d.*	n.d.*
400	2.5 ± 1.6	2.3 ± 1.4	2.4 ± 1.5
	247 ± 173	528 ± 431	672 ± 597
800	2.4 ± 1.4	2.8 ± 1.7	201± 139
	487.3 ± 682.0	744 ± 1045	3723 ± 1819

*n.d. = not detected.

(cac' = 508 μM). It should also be noted that the RLS spectrum, acquired under resonance conditions, is indicative of the absorption spectrum of aggregated species (λ_{max} = 360 nm) that is shifted to longer wavelengths with respect to the absorption spectrum of the peptide monomer (Figure SI1).

The CIGB-814 aggregation process was also studied using DLS. Fresh aqueous solutions of CIGB-814 at different concentrations (6, 60, 400, and 800 μM) were characterized. The solutions were analyzed after 72 and 96 h. The average diameters of the species detected using DLS measurements under different experimental conditions are listed in Table 1. In all cases, the analyzed samples showed a polydispersity index higher than 0.4.

In particular, at the peptide concentrations of 6 μM and 60 μM and after 96 h, no detectable aggregates could be observed. In contrast, the peptide solutions at concentrations of 400 and 800 μM exhibited a bimodal distribution. Interestingly, at 400 μM, i.e., below cac', the diameter distribution peaked at 2.5 nm and 672 nm (96 h), whereas at 800 μM, i.e., above cac', the bimodal distribution centered at 201 nm and 3.72 μm (96 h).

Figure SI6 shows the particle diameter distribution of the 800 μM sample at 0, 72, and 96 h.

Taken together, these results revealed that the aggregation process takes place through three different steps: i) 2–10 μM region: formation of CIGB-814 oligomers, as evidenced by fluorescence anisotropy measurements; ii) 10–123 μM (cac): peptide nanostructures (pyrene assay and CD spectra); iii) 123–669 μM (cac' = 508 μM): formation of micrometric β-sheet structures (ThT assay, RLS, and DLS).

AFM studies

Spectroscopic experiments indicated that CIGB-814 undergoes a multistep aggregation mechanism that is strongly dependent on the concentration range investigated. These complex phenomena likely influenced the morphology of the peptide aggregates formed. To further investigate this aspect, we performed AFM experiments after deposition of a CIGB-814 solution at a concentration of 33.5 μM on mica. AFM imaging revealed the presence of peptide globular structures, characterized by diameters ranging from 200 to 300 nm (Fig. 5). This finding is consistent with the pyrene assay measurements, indicating the presence of hydrophobic domains in the peptide nanostructures formed.

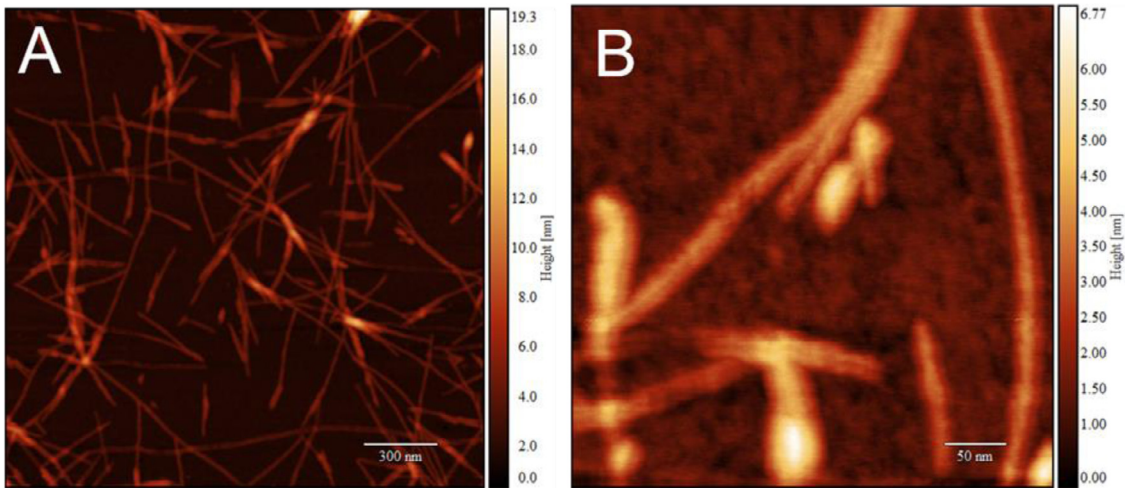

Fig. 6. AFM imaging of CIGB-814 on mica. Deposition solution concentration: 1.8 mg/mL (≈600 μM). Scale bar: 500 nm (left); 100 nm (right).

After deposition of an aqueous solution of CIGB-814 (1.8 mg/mL at 600 μM) on mica, peptide nanoaggregates with fibrillar morphology were observed (Fig. 6) [39].

The width and thickness of the peptide fibers imaged using AFM (Figure SI7) were 18.4 ± 0.5 nm, and 2.2 ± 0.2 nm, respectively. The length of the fibers ranged from 45 to 470 nm, with an average length of 321 ± 13 nm. Filaments formed by two intertwined fibrils, characterized by a width of 63 ± 9 nm, were also observed from the width distribution analysis of the peptide fibers [40].

These results strongly support the idea that at higher concentrations fibrillization of the peptide aggregates occurs, likely promoted by the formation of extended β-sheet structures (ThT assay).

Table 2
Radii of the equivalent sphere (R) and rotational correlation times (ϑ) of CIGB-814 monomers, trimers, hexamers and nonamers.

Oligomer	R (nm)	ϑ (ns)
1	0.83	0.52
3	1.20	1.55
6	1.51	3.10
9	1.73	4.64

3.2. MD simulations

MD simulations represent a valuable tool for investigating the structural and dynamical properties of peptides under different experimental conditions, with limitations on the dimensions of the systems that can be studied owing to the required computational time. Peptide aggregation may involve thousands of molecules, and the time required for efficient sampling is usually outside the accessible range. However, the aggregation of tens of peptides can be easily simulated, enabling the observation of the early stage of aggregation when peptide oligomers are formed. In addition, considering the hierarchical nature of peptide aggregation, MD simulations may provide a deeper understanding of the structural properties of higher-order aggregates [41,42]. In this context, MD simulations were performed in the presence of one (MD1), three (MD3), six (MD6), and nine (MD9) replicas of CIGB-814. First, a structural cluster analysis was performed using the root mean square deviation as a similarity criterion to identify the representative structures from each simulation. In this analysis, a cutting edge of 0.5 nm was applied, and the radius of gyration and the solvent accessible surface area (SASA) were considered as stability parameters. Representative structures of the most populated clusters of MD1 (A) and MD9 (B, C, and D) of the whole ensemble are shown in Fig. 7, whereas the representative structures from the cluster analysis of MD3 and MD6 are reported in Figures SI8 and SI9, respectively.

The cluster structures reported in Fig. 7 show predominant unordered conformations for both the monomer and nonamer simulations. However, in the latter case, some tracts of ordered structures, that is, short-β sheet segments, are present. By looking at the 3D shape of the aggregates, they span from globular (panels B and C in Fig. 7) to quite elongated profiles (panel D in Fig. 7), suggesting that different morphologies of the higher-order aggregates are possible. In agreement with the visual inspection of the representative structures, DSSP analysis revealed a slight increase in β structures (β-sheet and β-bridge contributions) of the oligomers with respect to the monomer, corresponding to the decrease in coil percentages upon aggregation (Figure SI10), in fair agreement with the CD results. This finding suggests that the aggregation process may structure disordered domains by promoting peptide interchain interactions.

To identify the amino acids involved in the stabilization of the aggregates, we examined the SASA values associated with the different residues. SASA analysis carried out on the MD3, MD6, and MD9 simulations (Figure SI11) revealed that the nonpolar residues, in particular Leu(4), Tyr(8), Leu(15), Val(16), Leu(18), Val(19), and Ala(20), showed a larger decrease in solvent accessibility (between −40 and −50%) with respect to the solvent accessibility of the same residues when the peptides were considered as isolated. This finding suggests that hydrophobic effects play an important role in the aggregation process. Furthermore, careful inspection of the data reported in Figure SI11 reveals that the average SASA decrease follows the trend MD9 > MD6 > MD3, confirming the increasing compact morphology of higher-order peptide clusters.

It should be noted that electrostatic interactions between charged side chains contribute significantly to the stability of CIGB-814 oligomers by forming transient salt bridges, as shown by the frequency map of contacts between the charged centers of the Asp-Lys-and Glu-Lys-pair sidechains occurring with a frequency higher than 2% in the nonamer aggregate MD frames (Figure SI12). Each barrel in Figure SI12 signals the proximity of a N^+—O^- pair at a distance less than or equal to 3.2 Å along the MD trajectory.

By applying an equivalent sphere representation of the most representative cluster structures obtained from MD1, MD3, MD6, and MD9, theoretical rotational correlation times (per molecule) ϑ can be obtained using the Einstein-Smoluchowski equation (Table 2):

$$\vartheta = \frac{\eta V}{kT}$$

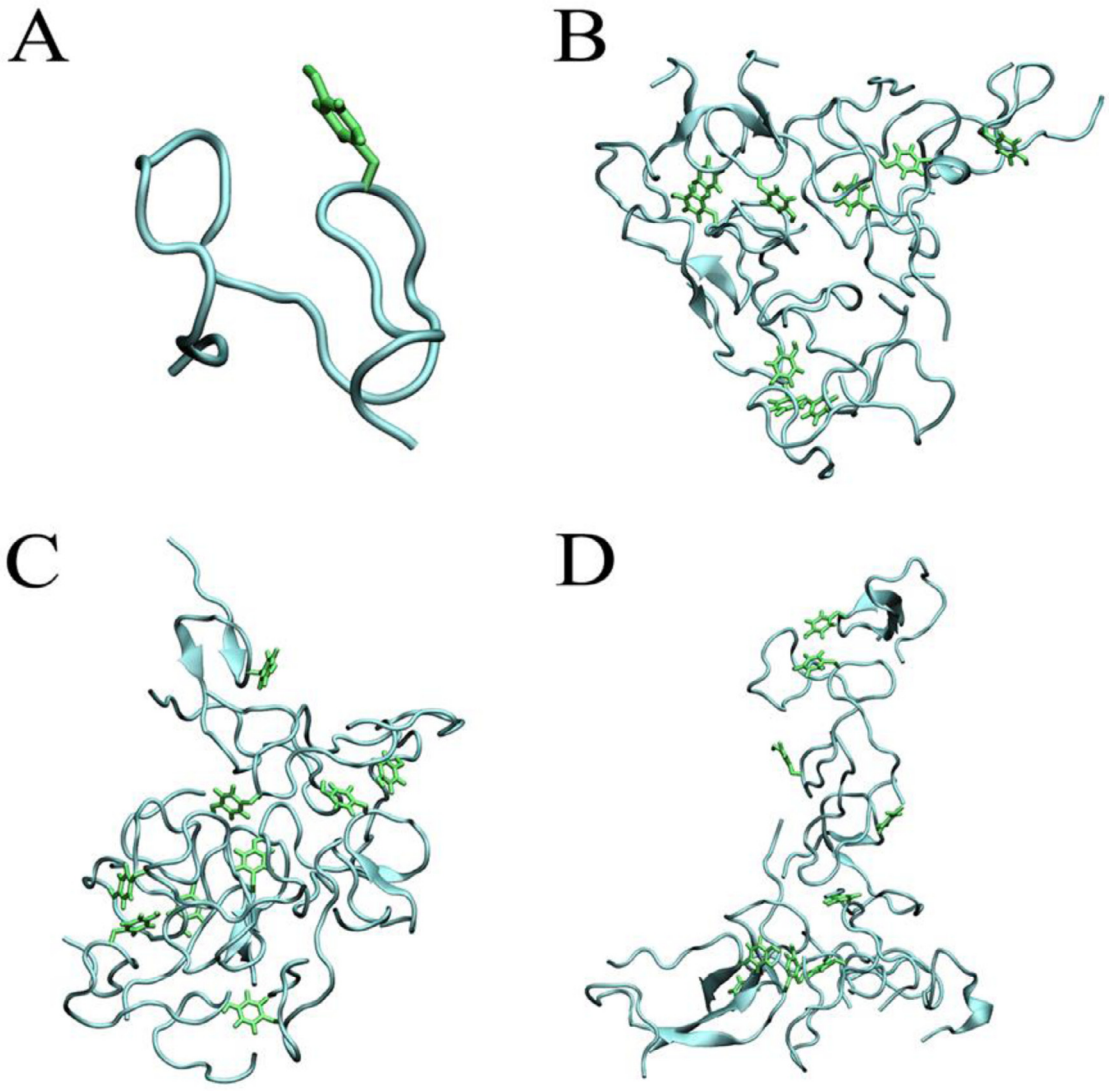

Fig. 7. Representative structures of the most populated clusters from molecular dynamics simulations of the monomer (A, 98%) and the nonamer [B(37%), C (38%), D(20%)] of CIGB-814 in 10 mM NaCl aqueous solutions.

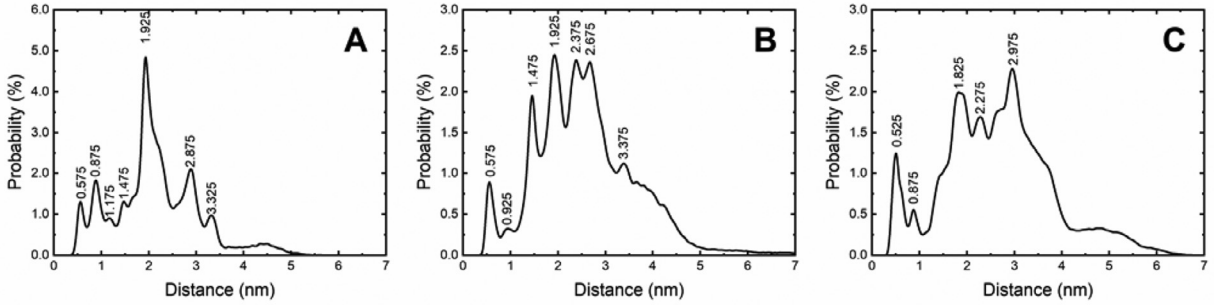

Fig. 8. Tyr-Tyr-distance distribution in CIGB-814 trimer (A), hexamer (B) and nonamer (C) from MD3, MD6 and MD9 cluster analysis.

where η is the viscosity, T is the temperature, and V is the hydrodynamic volume of the (spherical) rotating unit.

Of note, the rotational correlation times provided by the MD simulations are shorter than the rotational times derived from the experimental fluorescence anisotropy coefficients under the same spherical rotor approximation (Table SIT3). This discrepancy is most likely due to the local mobility of the tyrosine side chain, which significantly depolarizes the fluorescence anisotropy, causing a marked shortening of the experimental rotational correlation times. This finding distinctly emphasizes the dynamic nature of the CIGB-814 aggregates, in which the Tyr-groups maintain a relatively high mobility.

By looking at the representative structures of the peptide clusters (Figs. 7, SI8, and SI9), a heterogeneous picture emerges. Some Tyr-residues appear well embedded into the core of the aggregates; however, solvent-exposed Tyr-residues are also present. Interestingly, some direct interchain Tyr-Tyr-interactions can be easily identified, sometimes with

a distinct tendency to adopt a stacked configuration between the phenolic ring [41]. To better illustrate these aspects, Fig. 8 shows the Tyr-Tyr-distance distributions obtained by summing over the frequency of all the Tyr-Tyr-pair distances in the trimer (three Tyr-Tyr-pair distances), hexamer (15), and nonamer (36) peptide aggregates. It can be easily seen that for all three distributions, frequency peaks appear at well-defined Tyr-Tyr-distances. It should also be noted that some peaks occur at the same Tyr-Tyr-pair distances in all three distributions, indicating that a similar morphology occurs in aggregates of different dimensions. Most likely, Tyr-Tyr-residues positioned at distances less than 3 Å contribute to the stabilization of CIGB-814 aggregates by $\pi-\pi$ stacking interactions.

4. Conclusions

Peptide aggregation and fibrillation are driven by several concomitant factors, including peptide concentration, net charge, hydrophobic/hydrophilic balance, solution ionic strength, and pH [43]. Recent clinical studies have shown that peptide aggregation is key to determining the effective pharmacokinetics and pharmacodynamics of peptide-based drugs.

In this study, we investigated the aggregation properties of CIGB-814 using optical spectroscopy, DLS, AFM, and MD simulations.

We found that the CIGB-814 aggregation pathway is characterized by a multistep process that is strongly dependent on the peptide concentration. At micromolar concentrations, fluorescence experiments and MD simulations revealed the formation of nanometric peptide oligomers, leading to stable, compact structures when the number of peptide building blocks increased to 9. These structures are stabilized by interactions between hydrophobic residues, as revealed by the SASA analysis of MD simulations.

At concentrations higher than 100 μM, the pyrene assay indicated the formation of peptide nanostructures (cac = 123 μM), which could be imaged using AFM. These aggregates showed a globular morphology typical of an aggregation process driven by a hydrophobic effect. The analysis of transient contacts between charged side-chain groups revealed that electrostatic interactions also contributed significantly to the stabilization of peptide oligomers.

At concentrations greater than 500 μM, the coalescence of globular structures leads to the formation of peptide fibrils of micrometric length, as imaged using AFM and indicated by RLS and DLS measurements. The ThT assay allowed us to determine the critical concentration for such morphological transition (cac' = 508 μM), whereas CD analysis allowed us to detect secondary structure rearrangements of the peptide.

These findings may improve our understanding of CIGB-814 therapeutic activity in RA. The fine control over the morphology and size of CIGB-814 nanostructures could represent an innovative approach for modulating the efficiency and pharmacokinetics of CIGB-814.

Supplementary Information UV–Vis absorption and fluorescence measurements of CIGB-814 in water; diameter distribution of CIGB-814 aggregates from DLS experiments; size distribution of the CIGB-814 fibers from AFM measurements; and MD simulations of CIGB-814 oligomers (Cluster, DSSP, and SASA analysis).

Acknowledgement

This project received funding from the European Union Horizon 2020 Research and Innovation Program under the Marie Skłodowska-Curie grant agreement no. 872233 (“PEPSA-MATE”). GB acknowledges CINECA and the EU-PRACE program for the CPU time. FC acknowledges the funding received as an award of an RMIT senior vice chancellor fellowship.

Supplementary materials

Supplementary material associated with this article can be found, in the online version, at doi:10.1016/j.chphma.2021.09.007.

References

[1] F.C. Breedveld, M.H. Weisman, A.F. Kavanaugh, S.B. Cohen, K. Pavelka, R. van Vollenhoven, J. Sharp, J.L. Perez, G.T. Spencer-Green, The PREMIER study: a multicenter, randomized, double-blind clinical trial of combination therapy with adalimumab plus methotrexate versus methotrexate alone or adalimumab alone in patients with early, aggressive rheumatoid arthritis who had not had previous methotrexate treatment, Arthritis Rheum. 54 (2006) 26–37, doi:10.1002/art.21519.
[2] A. Rubbert-Roth, Assessing the safety of biologic agents in patients with rheumatoid arthritis, Rheumatology 51 (2012) 38–47, doi:10.1093/rheumatology/kes114.
[3] M.L. Toh, P. Miossec, The role of T cells in rheumatoid arthritis: new subsets and new targets, Curr. Opin. Rheumatol. 19 (2007) 284–288, doi:10.1097/BOR.0b013e32805e87e0.
[4] E. Zonneveld-Huijssoon, S. Albani, B.J. Prakken, F. Van Wijk, Heat shock protein bystander antigens for peptide immunotherapy in autoimmune disease, Clin. Exp. Immunol. 171 (2013) 20–29, doi:10.1111/j.1365-2249.2012.04627.x.
[5] F. Ishikawa, M. Kondo, T. Kakiuchi, The Role of IL-17 and related cytokines in inflammatory autoimmune diseases, Hindawi mediators of inflammation 2017 (2017), doi:10.1155/2017/3908061.
[6] D. Prada, L. Norailys, O. Corrales, A. López, E. González, A. Cabrales, Y. Reyes, Y. Bermudez, Y. Avila, L. Pérez, C. Molinero, O. Martinez, D.L. Oramas, Y. Miñoso, Y. Ramos, H. Garay, M. López, O. Reyes, H.M. Domínguez, Phase I clinical trial with a novel altered peptide ligand derived from human heat-shock protein 60 for treatment of rheumatoid arthritis: safety, pharmacokinetics and preliminary therapeutic effects, J. Clin. Trials. 8 (2018) 2–11, doi:10.4172/2167-0870.1000339.
[7] O. Corrales, L. Hernandez, D. Prada, Y. Reyes, A.M. López, L.J. González, H.M. Del Carmen Domínguez, CIGB-814, An altered peptide ligand derived from human heat-shock protein 60, decreases anti-cyclic citrullinated peptides antibodies in patients with rheumatoid arthritis, Clin. Rheumatol. 38 (2019) 955–960, doi:10.1007/s10067-018-4360-3.
[8] A. Cabrales-Rico, Y. Ramos, V. Besada, M. Del Carmen Domínguez, N. Lorenzo, O. García, J. Alexis, D. Prada, Y. Reyes, A.M. López, Y. Masforrol, H. Garay, L.J. González, Development and validation of a bioanalytical method based on LC–MS/MS analysis for the quantitation of CIGB-814 peptide in plasma from Rheumatoid Arthritis patients, J. Pharm. Biomed. Anal. 143 (2017) 130–140, doi:10.1016/j.jpba.2017.05.030.
[9] A.K. Banga, Therapeutic Peptides and Proteins, 2nd ed., Taylor & Francis, Boca Raton, FL, 2006.
[10] C.J. Roberts, Therapeutic protein aggregation: mechanisms, design, and control, Trends Biotechnol. 32 (2014) 372–380, doi:10.1016/j.tibtech.2014.05.005.
[11] K.L. Zapadka, F.J. Becher, L.G. dos Santos, S.E. Jackson, Factors affecting the physical stability (aggregation) of peptide therapeutics, Interface Focus 7 (2017) 20170030, doi:10.1098/rsfs.2017.0030.
[12] J.E. Gillam, C.E. MacPhee, Modelling amyloid fibril formation: mechanisms of nucleation and growth, J. Phys. Condens. Matter. 25 (2013) 373101, doi:10.1088/0953-8984/25/37/373101.
[13] A.K. Dey, P. Malyala, M. Singh, Physicochemical and functional characterization of vaccine antigens and adjuvants, Expert Rev. Vaccines. 13 (2014) 671–685, doi:10.1586/14760584.2014.907528.
[14] A. Levin, T.A. Hakala, L. Schnaider, G.J.L. Bernardes, E. Gazit, T.P.J. Knowles, Biomimetic peptide self-assembly for functional materials, Nat. Rev. Chem. 4 (2020) 615–634, doi:10.1038/s41570-020-0215-y.
[15] G.B. Fields, R.L. Noble, Solid phase peptide synthesis utilizing 9-fluorenylmethoxycarbonyl amino acids, Int. J. Pept. Protein Res. 35 (1990) 161–214, doi:10.1111/j.1399-3011.1990.tb00939.x.
[16] K. Kalyanasundaram, J.K. Thomas, Environmental effects on vibronic band intensities in pyrene monomer fluorescence and their application in studies of micellar systems, J. Am. Chem. Soc. 99 (1977) 2039–2044, doi:10.1021/ja00449a004.
[17] J.R. Lakowicz, Principles of Fluorescence Spectroscopy, 3rd ed., Springer Science & Business Media, New York, 2006.
[18] B. Pispisa, C. Mazzuca, A. Palleschi, L. Stella, M. Venanzi, M. Wakselman, J.-.P. Mazaylerat, M. Rainaldi, F. Formaggio, C. Toniolo, A combined spectroscopic and theoretical study of a series of conformationally restricted hexapeptides carrying a rigid binaphthyl-nitroxide donor-acceptor pair, Chem. Eur. J. 9 (2003) 4084–4093, doi:10.1002/chem.200304727.
[19] H.J.C. Berendsen, D. van der Spoel, R. van Drunen, GROMACS: a message-passing parallel molecular dynamics implementation, Comp. Phys. Comm. 91 (1995) 43–56, doi:10.1016/0010-4655(95)00042-E.
[20] N. Schmid, A.P. Eichenberger, A. Choutko, S. Riniker, M. Winger, A.E. Mark, W.F. van Gunsteren, Definition and testing of the GROMOS force-field versions 54A7 and 54B7, Eur. Biophys. J. 41 (2011) 843–856, doi:10.1007/s00249-011-0700-9.
[21] G. Bussi, D. Donadio, M. Parrinello, Canonical sampling through velocity rescaling, J. Chem. Phys. 126 (2007) 014101 https://aip.scitation.org/doi/abs/10.1063/1.2408420.
[22] M. Parrinello, A. Rahman, Polymorphic transitions in single crystals: a new molecular dynamics method, J. Appl. Phys. 52 (1981) 7182–7190 https://aip.scitation.org/doi/abs/10.1063/1.328693.
[23] T. Darden, D. York, L. Pedersen, Particle mesh Ewald: an N·log(N) method for Ewald sums in large systems, J. Chem. Phys. 98 (1993) 10089–10092 https://aip.scitation.org/doi/abs/10.1063/1.464397.
[24] B. Hess, H. Bekker, H.J.C. Berendsen, J.G.E.M. Fraaije, LINCS: a linear constraint solver for molecular simulations, J. Comput. Chem. 18 (1997) 1463–1472 https://doi.org/10.1002/(SICI)1096-987X(199709)18:12<1463::AID–JCC4>3.0.CO;2-H.
[25] A. Pedretti, L. Villa, G. Vistoli, VEGA—An open platform to develop chemo-bio-informatics applications, using plug-in architecture and

script programming, J. Comput. Aided. Mol. Des. 18 (2004) 167–173, doi:10.1023/B:JCAM.0000035186.90683.f2.
[26] W. Kabsch, C. Sander, Dictionary of protein secondary structure: pattern recognition of hydrogen-bonded and geometrical features, Biopolymers 22 (1983) 2577–2637, doi:10.1002/bip.360221211.
[27] H. Mach, C.R. Middaugh, R.V. Lewis, Statistical determination of the average values of the extinction coefficients of Tryptophan and Tyrosine in native proteins, Anal. Biochem. 200 (1992) 74–80, doi:10.1016/0003-2697(92)90279-G.
[28] L. Piñeiro, M. Novo, W. Al-Soufi, Fluorescence emission of pyrene in surfactant solutions, Adv. Colloid. Interface Sci. 215 (2015) 1–12, doi:10.1016/j.cis.2014.10.010.
[29] I.W. Hamley, S. Kirkham, A. Dehsorkhi, V. Castelletto, J. Adamcik, R. Mezzenga, J. Ruokolainen, C. Mazzuca, E. Gatto, M. Venanzi, E. Placidi, P. Bilalis, H. Iatrou, Self-Assembly of a model peptide incorporating a hexa-histidine sequence attached to an oligoalanine sequence, and binding to Gold NTA/Nickel Nanoparticles, Biomacromolecules 15 (2014) 3412–3420, doi:10.1021/bm500950c.
[30] L.S. Wolfe, M.F. Calabrese, A. Nath, D.V. Blaho, A.D. Miranker, Y. Xiong, Protein-induced photophysical changes to the amyloid indicator dye Thioflavine T, Proc. Natl. Acad. Sci. USA 107 (2010) 16683–16688, doi:10.1073/pnas.1002867107.
[31] M. Biancalana, K. Makabe, A. Koide, S. Koide, Molecular mechanism of Thioflavine T binding to the surface of beta-rich peptide self-assemblies, J. Mol. Biol. 385 (2009) 1052–1063, doi:10.1016/j.jmb.2008.11.006.
[32] M. Caruso, E. Gatto, E. Placidi, G. Ballano, F. Formaggio, C. Toniolo, D. Zanuy, C. Aleman, M. Venanzi, A single-residue substitution inhibits fibrillization of Ala-based pentapeptides. A spectroscopic and molecular dynamics investigation, Soft Matter 10 (2014) 2508–2519, doi:10.1039/C3SM52831F.
[33] W.R. Laws, J.B.A. Ross, H.R. Wyssbrod, J.M. Beechem, L. Brand, J.C. Sutherland, Time-resolved fluorescence and proton NMR studies of tyrosine and tyrosine analogs: correlation of NMR-determined rotamer populations and fluorescence kinetics, Biochemistry 25 (1986) 599–607, doi:10.1021/bi00351a013.
[34] B. Pispisa, A. Palleschi, L. Stella, M. Venanzi, C. Toniolo, A nitroxide derivative as a probe for conformational studies of short linear peptides in solution. Spectroscopic and Molecular Mechanics investigation, J. Phys. Chem. B. 102 (1998) 7890–7898, doi:10.1021/jp981415y.
[35] R.J. Turner, G.J. Moore, Long-lived fluorescence lifetime from tyrosine in a peptide derived from S- 100b, Biochim. Biophys. Acta. 1117 (1992) 265–270, doi:10.1016/0304-4165(92)90023-N.
[36] J.R. Lakowicz, G. Laczko, I. Gryczynski, Picosecond resolution of oxytocin tyrosyl fluorescence by 2 GHz frequency-domain fluorometry, Biophys. Chem. 24 (1986) 97–100, doi:10.1016/0301-4622(86)80002-3.
[37] X.Y. Jiang, X.Q. Chen, Z. Dong, M. Xu, The application of resonance light scattering technique for the determination of tinidazole in drugs, J. Autom. Methods Manage. Chem. (2007) 86857 2007, doi:10.1155/2007/86857.
[38] M. Caruso, E. Placidi, E. Gatto, C. Mazzuca, L. Stella, G. Bocchinfuso, A. Palleschi, F. Formaggio, C. Toniolo, M. Venanzi, Fibers or globules? Tuning the morphology of peptide aggregates from helical building blocks, J. Phys. Chem. B 117 (2013) 5448–5459, doi:10.1021/jp400009j.
[39] M. Savioli, L. Antonelli, G. Bocchinfuso, F. Cavalieri, R. Cimino, E. Gatto, E. Placidi, J.R.F. Massò, H. Garay Perez, H. Santana, M. Guerra-Vallespi, M. Venanzi, Formulation matters! A spectroscopic and molecular dynamics investigation on the peptide CIGB552 as itself and in its therapeutical formulation, J. Pept. Sci. (2021) e3356, doi:10.1002/psc.3356.
[40] S.K. Bhangu, G. Bocchinfuso, M. Ashokkumar, F. Cavalieri, Sound-driven dissipative self-assembly of aromatic biomolecules into functional nanoparticles, Nanoscale Horizons 5 (2020) 553–563, doi:10.1039/C9NH00611G.
[41] G. Bocchinfuso, P. Conflitti, S. Raniolo, M. Caruso, C. Mazzuca, E. Gatto, E. Placidi, F. Formaggio, C. Toniolo, M. Venanzi, A. Palleschi, Aggregation propensity of Aib homo-peptides of different length: an insight from molecular dynamics simulations, J. Pept. Sci. 20 (2014) 494–507, doi:10.1002/psc.2648.
[42] B.B. Gerbelli, S.V. Vassiliades, J.E.U. Rojas, J.N.B.D. Pelin, R.S.N. Mancini, W.S.G. Pereira, A.M. Aguilar, M. Venanzi, F. Cavalieri, F. Giuntini, W.A. Alves, Hierarchical Self-Assembly of Peptides and its Applications in Bionanotechnology, Macromol. Chem. Phys. 220 (2019) 1900085, doi:10.1002/macp.201900085.